

Structure and Catalysis of NiOOH: Recent Advances on Atomic Simulation

Ye-Fei Li,* Ji-Li Li, and Zhi-Pan Liu*

Cite This: *J. Phys. Chem. C* 2021, 125, 27033–27045

Read Online

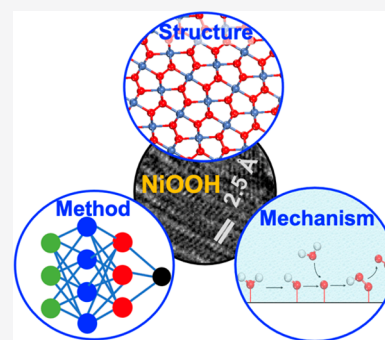
ACCESS |

Metrics & More

Article Recommendations

Supporting Information

ABSTRACT: NiOOH is one of the most promising catalysts for electrooxidation of water and organic molecules. Accompanying the long experimental practice to optimize the catalyst, atomic simulations, mainly based on density functional theory (DFT) calculations, have been performed in recent years to reveal the atomic structure of NiOOH and the reaction mechanism in catalysis. Due to both the structural complexity and the difficulty in computing the electronic structure, there are great concerns over the accuracy of first-principles methods and the validity of the structure models. This Perspective serves to overview the current status of atomic simulation on the structure and catalysis of NiOOH. We first present NiOOH phases and structures obtained by the latest global optimization methods in combination with machine learning potentials. The electronic structures of NiOOH are then described by comparing the performance of different theoretical levels, in particular, those based on PBE+U and hybrid functionals in DFT calculations. Finally, taking the oxygen evolution reaction of water splitting as the example, we elaborate the catalytic mechanism on pure, defective, and Fe-doped NiOOH surfaces and provide insights into the exceptional activity of the doped system. The further directions for theoretical investigations on NiOOH are also discussed.

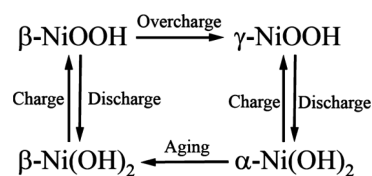


1. HISTORY ON NIOOH RESEARCH

NiOOH is a promising anode material for a series of important electrocatalytic oxidation reactions in the energy and catalysis sciences, such as the oxygen evolution reaction (OER),^{1,2} alcohol oxidation,³ and the urea oxidation reaction (UOR).^{4,5} For the OER, the key reaction in water splitting, the development of robust and efficient catalysts is a major challenge and NiOOH-based catalyst is shown to catalyze the OER at pH 14 with a high efficiency (10 mA/cm² at 0.3 V overpotential^{2,6}). The catalyst, however, still has a high overpotential and a poor long-term stability. To further optimize the catalyst, the in-depth mechanistic insight into the reactions on NiOOH is essential, which is, however, limited by the poor knowledge on the bulk phases and surface structures of NiOOH. Due to the complexity of electrochemical environment, the quality of experimental evidence, such as the X-ray diffraction patterns,⁷ is generally low in resolution. The theory for the structure–activity relationship of NiOOH is thus not established yet.

Since the publication of the first patents by Jünger (Ni/Cd)^{8,9} and Edison (Ni/Fe)¹⁰ in 1901, the NiOOH material was long used in alkaline batteries,^{11–13} which is generated from the brucite Ni(OH)₂ during charging (anode conditions). As shown by Bode's diagram in Scheme 1,¹⁴ the β-NiOOH phase is formed during charging, followed by γ-NiOOH under the overcharging conditions. It is generally agreed that both β- and γ-NiOOH are layered structures comprising NiO₂ sheets.¹⁵ The difference between the two phases comes from the Ni oxidation state and the intercalated species, where the

Scheme 1. Bode's Diagram for Ni(OH)₂–NiOOH Redox Transformations (Reprinted from Ref 16. Copyright 2014 American Chemical Society)



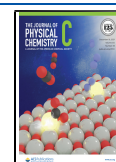
number and the position of H atoms (protons) in both phases are not resolved. For β-NiOOH, only protons are present in the interlayer space, while the interlayer space of γ-NiOOH is occupied by the protons, water molecules, and alkali metal cations. Based on a series of charging and discharging experiments on various forms of Ni(OH)₂, Barnard et al. concluded that the Ni oxidation state (OS) is 2.7–3.0 for β-NiOOH and 3.3–3.67 for γ-NiOOH,¹¹ which are not exactly +3, as indicated by the chemical formula.

From 1980s the research interests on NiOOH were renewed since it can exhibit good catalytic activity in electrochemical

Received: July 10, 2021

Revised: November 17, 2021

Published: December 6, 2021



oxidation reactions once the material is doped by the transitional metal, such as Fe,^{1,2} Co,^{17,18} Mn,¹⁹ Cr,²⁰ and Al.²¹ Among them, iron is perhaps the most investigated as the Fe impurities in nickel oxide electrodes were long known to facilitate the OER,^{22–25} a side reaction during the battery charging process. Recently, Bell et al. measured an overpotential of 0.529 V at 10 mA/cm² in the OER for a rigorously purified NiOOH, which, however, increases to 0.605 V after 3 days.² When using unpurified KOH solution containing trace amounts of Fe (≤ 0.66 ppm Fe), the overpotential decreases to 0.280–0.287 V at 10 mA/cm², and the NiOOH catalyst is found to contain more than 10% Fe near the surface after a five-day immersion.² In another study by Bell et al., the intentional Fe doping with 20–40 at. % Fe in NiOOH shows an overpotential of 0.275–0.300 V at 10 mA/cm².⁶ To date, Fe-doped NiOOH^{24,26} appears to be the most promising anode materials for the OER under alkaline conditions.

This Perspective provides a retrospective of the recent theoretical advances on NiOOH, focusing on the structure and the catalytic mechanism. Specifically, in section 2 we first briefly introduce the typical computational methods used to compute NiOOH. In section 3 we discuss the crystal structures and the electronic structures of NiOOH. In section 4, we elaborate the OER mechanism on pure, defective, and doped NiOOH surfaces. In section 5, we discuss the future directions for the atomic simulation of NiOOH.

2. METHODS ON NIOOH

2.1. Density Functional Theory Calculation Method.

Density functional theory (DFT) is the most widely used quantum mechanics method to determine the ground state total energy of system with the given atomic coordinates.^{27,28} DFT expresses the total energy as a functional of the electronic density $\rho(r)$ by

$$E[\rho(r)] = T[\rho(r)] + J[\rho(r)] + V_{\text{ext}}[\rho(r)] + E_{\text{xc}}[\rho(r)] \quad (1)$$

where T is the kinetic energy of ideal noninteracting electrons, J is the electron–electron Coulomb repulsion energy terms, V_{ext} is the potential energy of the nucleus–electron interaction, and E_{xc} is the exchange–correlation energy that describes all nonclassical corrections to the electron–electron interactions. The first three terms have an explicit mathematical formula while the last term lumps all of the most difficult many-body interaction terms and has no determined exact functional forms. Since the functional form has a huge impact on chemical reactivity prediction, considerable research efforts have been devoted in the past 40 years to improve the existing functionals and search for the exact functional form. In the field of heterogeneous catalysis, the most popular one is at the generalized-gradient-approximation (GGA) level in the form of Perdew–Burke–Ernzerhof (PBE)²⁹ functional.

NiOOH as a 3d metal oxide is a strongly correlated material and thus cannot be properly described by a standard DFT functional such as PBE. Most obviously, the standard DFT functionals tend to severely underestimate the band gap due to the delocalization error.³⁰ To overcome this drawback, the post-GGA functionals, e.g., PBE+U,³¹ PBE0,³² and HSE06,³³ have been developed. The computational cost of the PBE+U functional is comparable to the standard PBE functional, while PBE0 and HSE06 are hybrid functionals that have the computational cost significantly higher (e.g., 100 folds) than PBE+U.

For the PBE+U scheme as proposed by Dudarev et al.,³⁴ an effective parameter, the Hubbard term, $U_{\text{eff}} = U - J$, is introduced to the electron–electron interaction potential of Hamiltonian. The U_{eff} of Ni in NiOOH is in the range of 4.5–6.5 eV according to the linear response theory or via the fitting to experimental thermodynamic data.³⁵ As for the hybrid PBE0 and HSE06 functionals, a predefined amount of exact Hartree–Fock (HF) exchange is mixed with the PBE exchange. For PBE0 as an example, the exchange–correlation energy is given by

$$E_{\text{xc}}^{\text{PBE0}} = \alpha E_{\text{x}}^{\text{HF}} + (1 - \alpha)E_{\text{x}}^{\text{PBE}} + E_{\text{c}}^{\text{PBE}} \quad (2)$$

where E_{x}^{HF} is the exact exchange, $E_{\text{x}}^{\text{PBE}}$ is the PBE exchange, and $E_{\text{c}}^{\text{PBE}}$ is the PBE correlation. For HSE06, a screened Coulomb potential is applied to the exchange interaction in order to screen the long-range part of the exact exchange. A mixing coefficient $\alpha = 1/4$ is determined for both PBE0 and HSE06 by perturbation theory.³²

Recently, HSE06 with 15% exact exchange has also been used in modeling OER mechanisms on Fe-doped β -NiOOH. The parameter is taken directly from that used in iron oxides, which is shown to have the good performance for the energetics and electronic structures of iron oxides.³⁶ It is still not clear whether the choice of 15% exact exchange is also appropriate for pure β -NiOOH.³⁷

2.2. Solvation Models. There are three common approaches in the literature to account for the solvent effect for electrochemistry systems. The first approach is relatively simple, i.e., adding preconfigured 1–2 monolayer explicit water molecules on the NiOOH surfaces and not applying continuum solvation. Typically, only limited configurations of water molecules will be taken into account in exploring the possible pathways. This model may better capture the solvent effect of the first/second shell water molecules but completely omit the long-range electrostatic interaction in solution. While the error due to the missing of important configurations is the major concern in computation, these methods can produce definite total energy and the conventional reaction pathway search methods can be applied for finding intermediate states.

The second one is the continuum solvation model based on the modified Poisson–Boltzmann equation.^{38–41} The continuum solvation can describe the long-range polarization in solution, and in practice, a few explicit water layers may also be added in the framework to describe the short-range strong polarization due to solvation.

The third method is the explicit solvation model by adding a number of water layers on the surface with the realistic density. Long-time molecular dynamics (MD) simulation is generally involved to equilibrate the system for finding the free energy minimum. Obviously, this method is computationally very demanding, especially for DFT calculations. As a compromise, most current studies often carried out a short-time MD simulation and then selected a few low-energy snapshots as the structural models that are subject to reaction pathway calculations. Due to the statistic uncertainty of solvent shell as sampled from MD trajectories, it is important to verify the convergence of the final energetics, e.g., by considering more snapshots.

By including explicit water in the first shell and the continuum solvation model, Li and Liu show that the free energy change of the reaction $*\text{H}_2\text{O} \rightarrow *\text{OH} + \text{H}^+(\text{aq}) + \text{e}^-$ on γ -NiOOH (0112) is 0.70 eV.⁴² The value increases to 0.77 eV without the continuum solvation model, and if further

removing the explicit water, it becomes 0.89 eV. This demonstrates the appreciable magnitude of short-range and long-range solvation effect, and obviously, an overall magnitude of ~ 0.2 eV cannot be neglected. Vandichel et al. show an even larger effect of solvation: the free energy change of the reaction $*\text{H}_2\text{O} \rightarrow *\text{OH} + \text{H}^+(\text{aq}) + \text{e}^-$ on Fe-doped γ -NiOOH (01 $\bar{1}2$) is 1.12 eV with the explicit solvation model and it increases to 1.83 eV without the solvent water molecules.⁴³ The trend of free energy change is consistent with the different polarization of $*\text{OH}$ and $*\text{H}_2\text{O}$ in solution, where the $*\text{OH}$ state on the NiOOH surface, being more negatively charged, exhibits a stronger polarization than $*\text{H}_2\text{O}$.

3. CRYSTAL STRUCTURES FOR NIOOH

3.1. Proposed NiOOH Models. NiOOH has two possible bulk phases, β -NiOOH and γ -NiOOH. Both phases are active for the OER in experiments.^{44,45} There are, however, few experimental data available for their crystal structures. The structure of β -NiOOH can be considered as directly removing half the protons from β -Ni(OH)₂.¹⁵ But recent experimental evidence shows that some unsettled structures exist in the β -NiOOH crystal. For instance, Delahaye-Vidal et al. observed an irreversible microstructural transformation that produces mosaic textures during the first oxidation cycle from β -Ni(OH)₂ to β -NiOOH,⁴⁶ which is later confirmed by high-resolution transmission electron microscopy (HRTEM).⁷ Besides, Casas-Cabanas et al. identified a doubling of the *c* axis of β -NiOOH relative to β -Ni(OH)₂.⁷ By fitting the X-ray and neutron powder diffraction patterns, Casas-Cabanas et al. proposed a crystal structure that consists of NiO₂H sheets with “ABCA” stacking order.⁷ This structure is, however, not supported by recent DFT calculations and undergoes significant structural transformation after geometry relaxation.^{47,48} Therefore, a precise crystal structure of β -NiOOH has not been established yet.

As for γ -NiOOH, X-ray diffraction patterns show that all samples with dissimilar intercalated water and alkali cations contents have an analogous rhombohedral cell. Specifically, the lengths of *a* and *b* axes are similar, while the lengths of the *c* axis can be notably different. Thus, the experimental data suggest that γ -NiOOH is a layered structure that consists of NiO₂ sheets with “ABBCCA” stacking order,¹⁵ but the content and configuration of intercalated species for γ -NiOOH are still unclear.

In fact, a number of β -NiOOH crystal structures have been proposed by different research groups independently. Figure 1 structures a–e summarize the β -NiOOH structural models used in literatures.^{47,48} Apparently, all these models suppose a chemical formula of NiO₂H for β -NiOOH. In structure a, all protons are on the same side, forming a stoichiometric NiOOH layer. This structure corresponds to the directly remove half protons from the original β -Ni(OH)₂ and will hereafter be denoted as the native structure. In structure b, the protons segregate within the interlayer space, forming alternating Ni(OH)₂ and NiO₂ layers. This structure is denoted as the alternate structure.⁴⁸ In structure c, half of the intercalated protons evenly distribute on the opposite side of the NiO₂ sheet, the uniform structure.^{44,47} In structures d, every second proton is on the opposite side of the NiO₂ sheet, the staggered structure,⁴⁷ while in structure e, protons are also in the staggered configuration but with a different NiO₂ stacking ordering, the staggered-II structure. All the models except for the staggered-II structure share the same

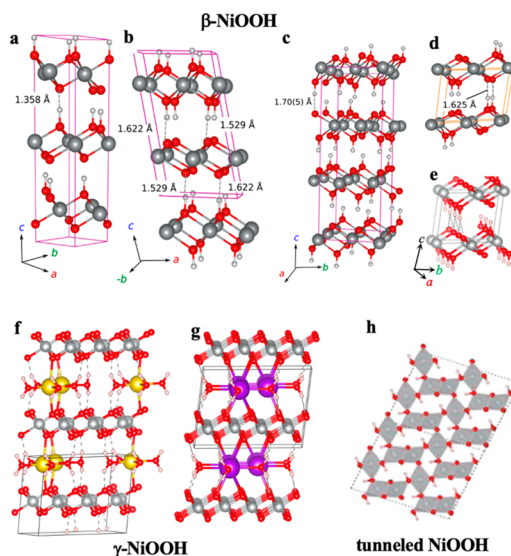


Figure 1. NiOOH structures proposed in the literature: (a–e) β -NiOOH; (f–g) γ -NiOOH; (h) tunneled NiOOH. Colors in the figure: gray balls are Ni; red balls are O; white balls are H; yellow balls are Na; purple balls are K. Reprinted from refs 47 and 48. Copyright 2018 and 2014 American Chemical Society.

“ABBCCA” stacking sequence for the NiO₂ sheets, while the staggered-II structure has a “ABB’CC’A” stacking order stacking where B’ is shifted by $1/2a$ along the crystal axis with respect to B.

By using DFT calculations with PBE+U functional and $U_{\text{eff}} = 5.5$ eV, Carter et al. show that the staggered structure is the most stable one, and the energies of the alternate and uniform structures are slightly higher (~ 0.02 eV/f.u.).⁴⁷ The native and staggered-II structures are least stable, being 0.10 and 0.15 eV/f.u. higher than the staggered structure, respectively.

As for γ -NiOOH, its structure is even more complicated than the β phase since it involves flexible water in the interlayer space. Based on the available experimental data, a crystal structure γ -NiOOH with a chemical formula of $\text{M}_{0.33}\text{NiO}_2 \cdot 0.67\text{H}_2\text{O}$ ($\text{M} = \text{Na}^+, \text{K}^+, \text{etc.}$) is proposed in the literature,^{16,49,50} as shown in Figure 1f (denoted as (2 × 3)-2M structure). In this model, two alkali metal cations intercalate between (2 × 3) NiO₂ layers, leading to a Ni OS of +3.66. In the optimized unit cell, the interlayer spacing is ~ 7.0 Å, well consistent with the experimental value of 7 Å.⁵¹ More recently, Strasser et al. performed a structural search for γ -NiOOH within a wide chemical formula from NiO₂ · 0.25H₂O to K_{0.33}NiO₂ · 1.33H₂O by using MD simulations.⁵² Their results show that the γ -NiOOH structure with four water molecules and two K⁺ cations intercalated between (2 × 4) NiO₂ layers is the most favorable in energy, as shown in Figure 1g. This (2 × 4)-2M structure has a Ni OS of +3.75 and an interlayer spacing of 7.2 Å.⁵² For both (2 × 3)-2M and (2 × 4)-2M models, the oxygen atoms of NiO₂ sheets follow the “ABBCCA” stacking sequence.

In addition to the above two models, the deprotonated β -NiOOH structure were also utilized to represent the γ -NiOOH.^{42,44} We denoted this structure as the simplified- β structure. In this model, a fraction of protons in β -NiOOH are removed to produce an average Ni OS close to the experimental value of +3.66. This model however neglects the role of intercalated species.

Besides the layered structure, Li and Selloni reported a series of metastable tunneled NiOOH structures isostructural with MnO₂ polymorphs, which were found by searching the structure of NiOOH using the genetic algorithm.⁴⁸ Figure 1h illustrates the most stable tunneled NiOOH, which has mixed (2 × 1) and (1 × 1) tunnels with protons inside the channels. The energy of the structures is only 0.06 eV/f.u. (PBE+U) higher than the staggered structure. They thus predicted that the tunneled structure might also exist in some reconstructed regions of β-NiOOH.⁴⁸ Later, Mai et al. indeed observed a tunneled NiOOH phase in experiment by using the lithiation-induced pulverization strategy.⁵³ To summarize, the bulk structure of NiOOH is still far from being settled, and new theoretical and experimental techniques are called for to resolve the atomic structures.

3.2. Phase Diagram of β-NiOOH by SSW-NN. Since 2017 our group developed a machine-learning based global optimization method, namely, the SSW-NN method as implemented in the LASP program,^{54–59} which can be utilized to predict the structure of complex materials. This method utilized the stochastic surface walking (SSW) method to sample the global potential energy surface, and the data collected by SSW are utilized to construct the global neural network (G-NN) potential. By iteratively training the potential, the G-NN can be finally established. There are already more than 200 different G-NN in the LASP program (see webpage www.lasphub.com). More details of the method can be found in our previous publications.^{54–59}

By using the Ni–O–H global NN potential, the global potential energy surface of β-NiOOH at a series of stoichiometries, NiO₂H_x (x = 0–2), have been explored by SSW within the supercell of 12 Ni atoms, i.e., Ni₁₂O₂₄H_(12×x). After further confirming the low-energy structures using DFT (PBE+U, U_{eff} = 5.5 eV), the free energies of the phases at different electrochemical potentials are obtained and summarized in Figure 2. Interestingly, a new β-NiOOH structure is identified, which is 0.02 eV/f.u. lower than the previously most stable structure, the staggered structure in Figure 1d. This new

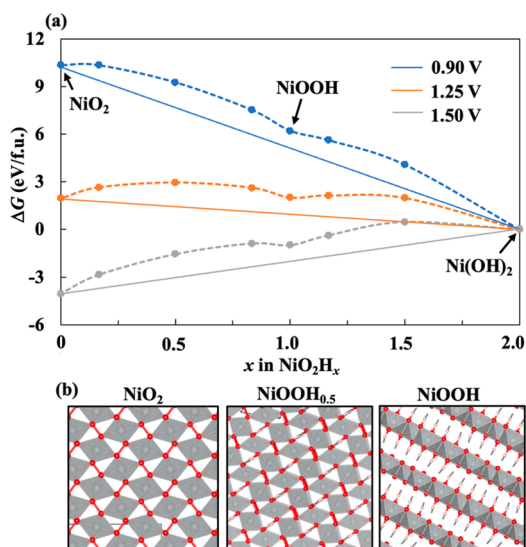
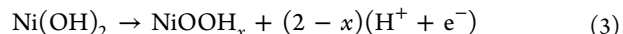


Figure 2. (a) Convex hull diagram of NiO₂H_x at U = 0.90, 1.25, and 1.50 V vs RHE. (b) Global minima of NiO₂, NiOOH_{0.5}, and NiOOH. Colors in the figure: red balls are O; gray balls are Ni; white balls are H. The dashed lines in (b) represent the hydrogen bonds.

β-NiOOH structure has an alternate NiO₂ and Ni(OH)₂ local layer structures and both NiO₂ and Ni(OH)₂ domains are present within a single NiO₂ layer. For the other compositions, NiO₂H_x, they maintain the layered structure when x > 0.5 and when x < 0.5, a tunneled structure that has never been reported in the literature is identified. This new structure features the peroxo O–O bonding between lattice O atoms (see NiO₂ in Figure 2b).

The convex hull diagram for NiOOH phases can then be computed by using the overall reaction, eq 3.



As shown in Figure 2, the β-NiOOH is in fact not a convex point in the diagram, indicating this phase tends to decompose into β-Ni(OH)₂ and tunneled NiO₂ in thermodynamics. In particular, above 1.25 V vs reversible hydrogen electrode (RHE), the typical operating condition for the OER, the tunneled NiO₂ turns out to be thermodynamically more stable than β-NiOOH. It is interesting to further confirm the existence of this new phase in the future studies, both by experiment and advanced computational methods.

3.3. Electronic Structures of Bulk NiOOH. Due to the great uncertainty of the geometrical structure, the electronic structure of NiOOH is also not concluded. It is known from experiment that the NiOOH is a semiconductor with a band gap of 1.7–1.8 eV.⁶⁰ The X-ray photoelectron spectroscopy (XPS) results suggest that, apart from Ni³⁺ and Ni⁴⁺ ions, there is Ni²⁺ ions in NiOOH.⁶¹ There is little information on the other electronic properties, such as spin ordering.

To reveal the electronic structure of NiOOH, Li and Selloni calculated the density of states (DOS) for alternate β-NiOOH by PBE+U, PBE0, and HSE06 functionals, as shown in Figure 3.⁴⁸ The PBE+U functional predicts that both β- and γ-NiOOH are half-metallic with a ferromagnetic (FM) configuration, where no band gap exists in the majority spin-up component. This result indicates the DFT+U scheme is unable to correctly predict the electronic structure of β-NiOOH. In contrast, the hybrid HSE06 and PBE0 functionals successfully predict band gaps of 1.5 and 2.5 eV. More recently, Carter et al. report a band gap of 1.96 eV by using a G₀W₀ calculation on the staggered-II β-NiOOH, confirming the acceptable accuracy for hybrid functionals (HSE06 and PBE0) to open the band gap.⁶²

Apart from the band gap, the oxidation state (OS) of Ni is another important property for NiOOH. Since the Ni cation is always in the octahedral coordination and thus the Ni⁽²⁺ⁿ⁾⁺ ion has a configuration of t_{2g}⁶e_g^{2–n} according to the crystal ligand field theory, one can derive the Ni OS from the on-site spin by using charge population analysis. Indeed, previous studies have shown that Ni⁴⁺ has zero net spin, and only the OS within Ni²⁺ to Ni³⁺ are spin-polarized with the net magnetic moment.^{42,48} Li and Selloni showed that the number and the arrangement of the intercalated proton and alkali metal cations could influence the local OS of Ni, giving rise to mixed Ni²⁺, Ni³⁺, and Ni⁴⁺.^{42,48}

By using DFT (PBE+U) calculations, Li and Selloni investigated the OS of Ni ions in the alternate β-NiOOH.⁴⁸ They found that Ni ions are not all Ni³⁺ but have three different spin moments, 0.9, 1.7, and 0 μ_B, with the relative populations of 2, 1, and 1. The ferromagnetic (FM) spin ordering is the ground state. This indicates the self-disproportionation occurs with a half of the Ni³⁺ cations changing to Ni²⁺/Ni⁴⁺ pairs (see Figure 3d). The calculation

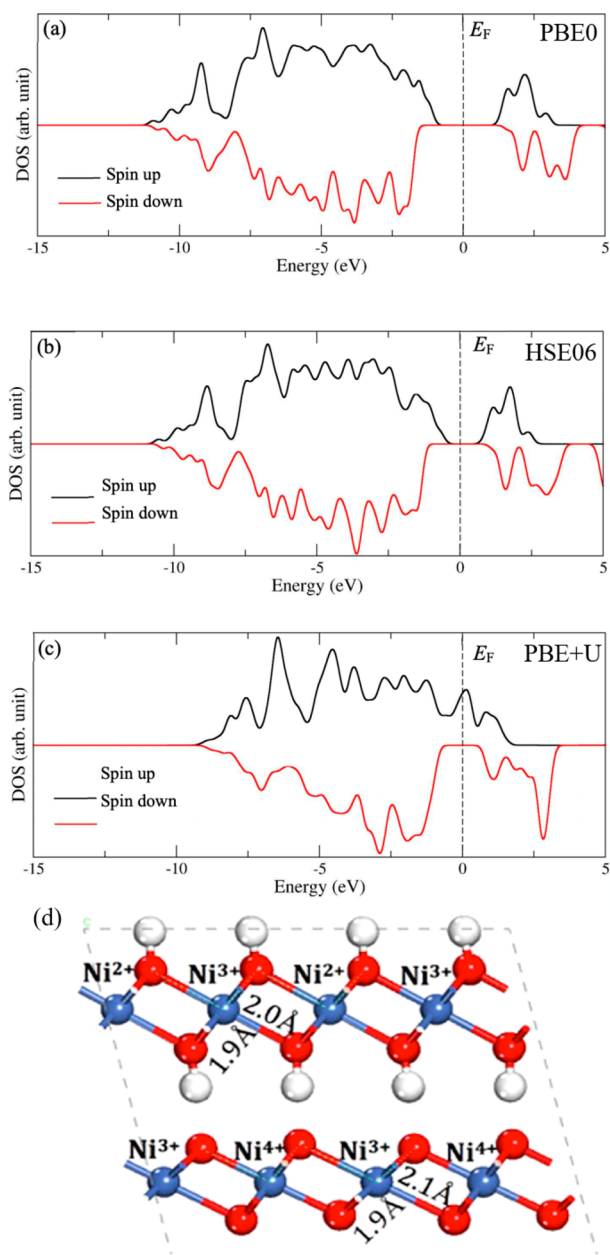


Figure 3. Electronic structures of alternate β -NiOOH. (a–c) The density of states with PBE0, HSE06, and PBE+U with $U_{\text{eff}} = 5.5$ eV. The dotted lines represent the Fermi level. (d) The OS and bond lengths of Ni ions. Reprinted from ref 48. Copyright 2014 American Chemical Society.

result agrees with the XPS observation that Ni^{2+} ions exist in NiOOH,⁶¹ which was suggested to originate from the disproportionation of Ni^{3+} .

Toroker et al. carried out an extensive benchmark study for the bulk geometry, OS, and band gap on the alternate β -NiOOH⁶⁵ by using PBE, PBE+U, DFT-vdW (optPBE, optB86, and optB88), hybrid functionals (HSE06 and PBE0), and DFT-D2 (HSE06-D2 and PBE0-D2) functionals. They show that the PBE+U functional is sufficient to generate reliable geometry and OS of NiOOH, although it fails to open the band gap. The benefit of DFT-vdW and DFT-D2 is marginal with regard to obtaining the accurate geometry.

In summary, the electronic structure of NiOOH is sensitive to the choice of DFT functionals. The hybrid functionals are

required in order to predict correctly the band structure. For the structural and redox properties, the low-cost PBE+U functional can already predict results that are consistent with experimental data.

3.5. Surfaces of NiOOH. The Miller–Bravais indices have been utilized to describe the surfaces of β - and γ -NiOOH based on their layered structure of NiO_2 sheets.^{32,34,36,40,41,45,47–49} The O atoms of the NiO_2 sheets are in the same “ABBCA” stacking order, and the symmetry of NiO_2 lattice is $R\bar{3}m$ with a C_3 axis perpendicular to the NiO_2 sheet, as shown in Figure 4a,b. The typical surface indices are

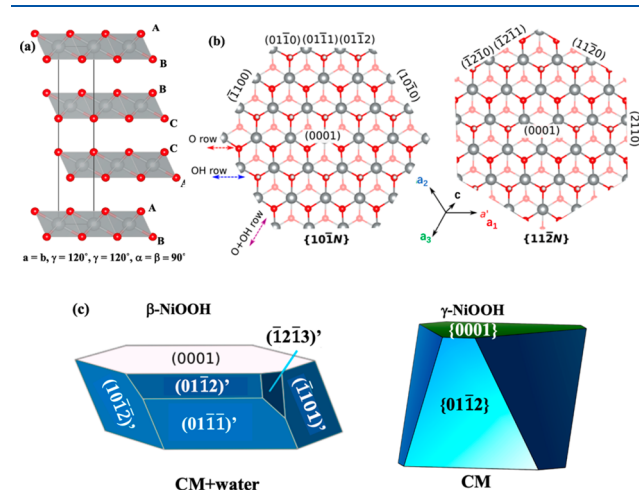


Figure 4. Miller–Bravais indices in a conventional hexagonal lattice. (a) The sublattice of NiO_2 sheets with a space group of hexagonal $R\bar{3}m$. (b) Definitions of the surface indices. (c) The Wulff shape of β - and γ -NiOOH. Red balls are O; gray balls are Ni; white balls are H. Reprinted from refs 47 and 42. Copyright 2018 and 2020 American Chemical Society.

summarized in Figure 4b. The (0001) face of NiOOH is the basal plane, where both Ni and O ions are fully coordinated, while for other facets, unsaturated Ni and O expose on the surface.

More generally, the $\{10\bar{1}N\}$ faces expose five-coordinated Ni (Ni^{5c}), O^{2c} , and O^{3c} on the bare surface, while the $\{1\bar{1}2N\}$ faces expose Ni^{4c} and O^{2c} . The fourth digit N in the indices does not change the termination of NiO_2 sheets, but only alters the offset of NiO_2 -sheet edges. Note that two surfaces with the same facet name means the identical termination of the NiO_2 sheet, but they may well be different in the intercalated species, e.g., H atoms and cations, which will break the 3-fold rotational symmetry.

We notice that the Miller–Bravais indices used in Carter’s works^{37,47,62,64–66} are different from those in other literature.^{5,8,10,11} To unify the nomenclature of crystal planes, we here transform the indices used in Carter’s works to the conventional ones. The correspondence between the two sets of indices is listed in the Supporting Information.

3.6. Surface Energies and Morphologies of NiOOH. Carter et al. have computed the stability of β -NiOOH surfaces by using the continuum solvation model with explicit water molecules (CM + water),⁴⁷ as shown in Table 1. Not surprisingly, the basal plane (0001) has the lowest surface energy of 0.192 J/m² where the layer–layer interaction is dominated by the weak hydrogen bonds, while the other facets have a notably higher surface energy of 0.445 – 0.609 J/m².

Table 1. Surface Energies of β - and γ -NiOOH in Aqueous Conditions

surface	surface CN _{Ni}	surface CN _O ^a	γ (J/m ²) ^b	
			CM	CM + water
β -NiOOH (Staggered Structure)				
(0001)	6	3	0.192	0.192
(10 $\bar{1}\bar{2}$)	5	2, 3	0.499	0.445
($\bar{1}$ 101)	5	2, 3	0.653	0.508
(01 $\bar{1}\bar{1}$)	5	2, 3	0.578	0.449
(01 $\bar{1}\bar{2}$)	5	2, 3	0.478	0.478
(01 $\bar{1}\bar{5}$)	5	2, 3	0.515	0.515
(11 $\bar{2}\bar{3}$)	4	2	0.981	0.579
($\bar{1}\bar{2}\bar{1}\bar{3}$)	4	2	1.043	0.533
(2 $\bar{1}\bar{1}\bar{3}$)	4	2	0.987	0.609
γ -NiOOH ((2 × 3)-2M Structure)				
(0001)	6	3	0.277	
(01 $\bar{1}\bar{2}$)	5	2,3	0.311	
(01 $\bar{1}\bar{0}$)	5	2,3	0.533	

^aCoordination number of O in the NiO₂ framework on the bare surface (CN_O). ^bData are from refs 47 and 42 for β - and γ -NiOOH, respectively.

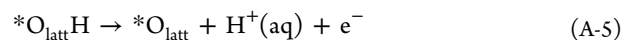
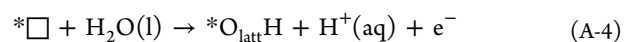
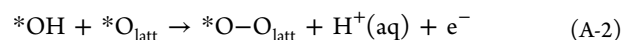
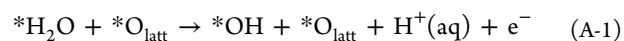
Therefore, the equilibrium β -NiOOH Wulff shape is predicted to be in the hexagonal platelet morphology dominated by (0001) surface, as shown in Figure 4c.⁴⁷ The (01 $\bar{1}\bar{2}$) surfaces are the major facet on the sidewalls and the (01 $\bar{1}\bar{2}$) and ($\bar{1}\bar{2}\bar{1}\bar{3}$) are also present as minority surfaces.⁴⁷

As for γ -NiOOH, our group recently calculated the surface energies of three selected low-index faces using the continuum solvation model (CM).⁴² We show that the surface energy of the basal plane (0001) is 0.277 J/m², higher than that of β -NiOOH. This is reasonable since the basal planes in γ -NiOOH are connected by relatively strong dative bonds between the intercalated alkali metal ions and the oxygens of NiO₂ sheets. As a result, the Wulff shape transforms to a distorted hexagonal prism (see Figure 4c).

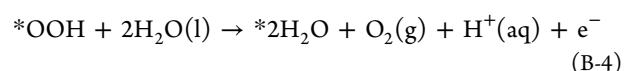
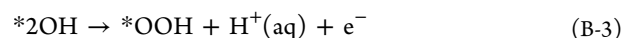
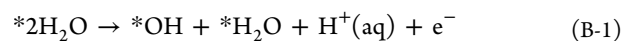
4. CATALYSIS

4.1. OER on Pure NiOOH. Now we are in the position to discuss the OER activities on NiOOH. The activity of NiOOH has been intensively studied by DFT calculations and numerous mechanisms have been proposed in the literature.^{37,38,42,65–68} These OER mechanisms can be generally divided into seven pathways, according to the intermediates. The elementary reactions involved are depicted in the following.

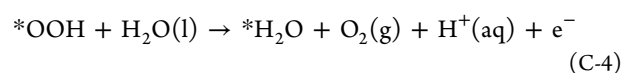
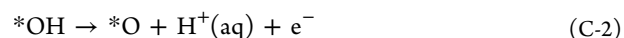
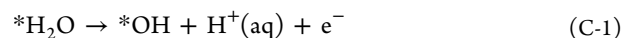
A. The “lattice peroxide” path:



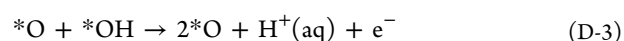
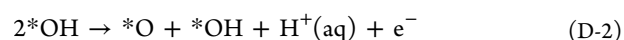
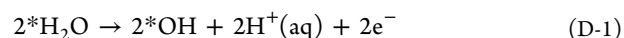
B. The “hydroperoxide” path:



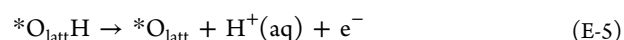
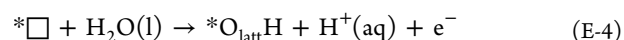
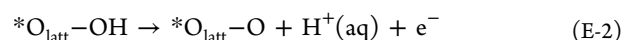
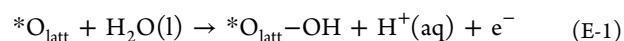
C. The “electrochemical metal peroxide” path:



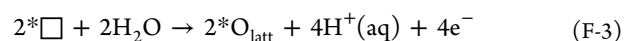
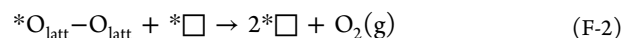
D. The “oxide” path:



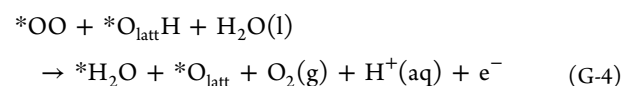
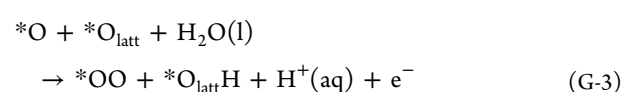
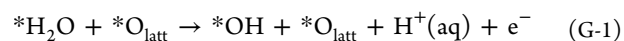
E. The “water nucleophilic attack” path:



F. The “lattice oxygen coupling” path:



G. The “bifunctional” path:



In the equations, the O_{latt} indicates the lattice O and * \square represents the surface O vacancy.

The most common method to calculate the OER activity is the computational hydrogen electrode (CHE) model.^{16,35,38,69–72} In this model, the OER activity can be estimated by the thermodynamic overpotential (η), which is defined as the most unfavorable Gibbs free energy change at the reversible potential of corresponding reaction ($U_{\text{OER}} = 1.23$ V vs RHE).

Table 2. Mechanism and Activity for the OER on NiOOH in the Literature

surface	mechanism	potential-determining step	η (V)	method ^a	structure	ref
β -NiOOH						
(01 $\bar{1}$ 5)	“lattice peroxide” path	*H ₂ O + \rightarrow *OH + H ⁺ (aq) + e ⁻	0.46	PBE+U(5.5)	uniform	16
(0001)	“oxide” path	*O + *OH \rightarrow 2*O + H ⁺ (aq) + e ⁻	0.52	PBE+U(5.5)+ CM	staggered-II	65
(0001)	“water nucleophilic attack” path	*O _{latt} H \rightarrow *O + H ⁺ (aq) + e ⁻	0.69	PBE+U(5.5)	staggered	37
(0001)	“water nucleophilic attack” path	*O _{latt} H \rightarrow *O + H ⁺ (aq) + e ⁻	0.44	ONIOM-HSE06(15%)	staggered	37
(10 $\bar{1}$ 2)	“lattice peroxide” path	*H ₂ O \rightarrow *OH + H ⁺ (aq) + e ⁻	0.64	PBE+U(5.5)	staggered	37
(10 $\bar{1}$ 2)	“lattice peroxide” path	*H ₂ O \rightarrow *OH + H ⁺ (aq) + e ⁻	0.43	ONIOM-HSE06(15%)	staggered	37
($\bar{1}$ 2 $\bar{1}$ 3)	hydroperoxide” path	*OH + *H ₂ O \rightarrow *2OH ⁺ H ⁺ (aq) + e ⁻	0.67	PBE+U(5.5)	staggered	64
($\bar{1}$ 2 $\bar{1}$ 3)	hydroperoxide” path	*OH + *H ₂ O \rightarrow *2OH ⁺ H ⁺ (aq) + e ⁻	0.80	ONIOM-HSE06	staggered	64
($\bar{1}$ 2 $\bar{1}$ 3)	hydroperoxide” path	*OH + *H ₂ O \rightarrow *2OH ⁺ H ⁺ (aq) + e ⁻	0.48	ONIOM-HSE06(15%)	staggered	64
(01 $\bar{1}$ 2)	“lattice peroxide” path	*H ₂ O \rightarrow *OH + H ⁺ (aq) + e ⁻	0.52	PBE+U(5.5)	unknown	76
(01 $\bar{1}$ 2)	“lattice peroxide” path	*O _{latt} H \rightarrow *O _{latt} + H ⁺ (aq) + e ⁻	0.53	PBE+U(5.5)+ CM	staggered	42
(01 $\bar{1}$ 2)	“lattice peroxide” path	*O _{latt} H \rightarrow *O _{latt} + H ⁺ (aq) + e ⁻	0.93	HSE06+CM	staggered	42
(0001)	“water nucleophilic attack” path	*O + H ₂ O(l) \rightarrow *OOH + H ⁺ (aq) + e ⁻	0.65	PBE+U(4.5)	staggered	77
(01 $\bar{1}$ 2)	“lattice peroxide” path	*OH + *O _{latt} \rightarrow *O-O _{latt} + H ⁺ (aq) + e ⁻	0.28	PBE+U(5.5)	uniform	78
(0001)	“water nucleophilic attack” path	*O + H ₂ O \rightarrow *OOH + H ⁺ (aq) + e ⁻	0.65	PBE-D3	unknown	79
(0001)	“water nucleophilic attack” path	*O _{latt} + H ₂ O \rightarrow *O _{latt} -OH + H ⁺ (aq) + e ⁻	0.57	PBE+U(5.5)	staggered-II	66
γ -NiOOH						
(01 $\bar{1}$ 5)	“lattice peroxide” path	*H ₂ O \rightarrow *OH + H ⁺ (aq) + e ⁻	0.52	PBE+U(5.5)	(1 \times 3)-2M	16
(01 $\bar{1}$ 2)	“electrochemical metal peroxide” path	*OH \rightarrow *O + H ⁺ (aq) + e ⁻	0.83	PBE	(1 \times 3)-2M	49
(01 $\bar{1}$ 2)	“electrochemical metal peroxide” path	*O + H ₂ O(l) \rightarrow *OOH + H ⁺ (aq) + e ⁻	0.56	RPBE+U(6.6)	simplified	44
(01 $\bar{1}$ 2)	“lattice peroxide” path	*H ₂ O \rightarrow *OH + H ⁺ (aq) + e ⁻	0.70	PBE+U(5.5)+ CM	simplified	42
(01 $\bar{1}$ 2)	“lattice peroxide” path	*H ₂ O \rightarrow *OH + H ⁺ (aq) + e ⁻	0.65	HSE06+CM	simplified	42
(01 $\bar{1}$ 2)	“electrochemical metal peroxide” path	*OH \rightarrow *O + H ⁺ (aq) + e ⁻	1.21	B3PW91+ CANDLE	(1 \times 3)-2M	50
(01 $\bar{1}$ 0)	“water nucleophilic attack” path	*H ₂ O \rightarrow *OH + H ⁺ (aq) + e ⁻	0.67	optPBE+U(5.2)	(1 \times 4)-2M	52
(0001)	“electrochemical metal peroxide” path	*O + H ₂ O(l) \rightarrow *OOH + H ⁺ (aq) + e ⁻	0.65	PBE+D3	native	79
(01 $\bar{1}$ 2)	“electrochemical metal peroxide” path	*OH \rightarrow *O + H ⁺ (aq) + e ⁻	0.65	BEEF-vdW	(1 \times 3)-2M	43
(01 $\bar{1}$ 2)	“electrochemical metal peroxide” path	*H ₂ O \rightarrow *OH + H ⁺ (aq) + e ⁻	0.58	BEEF-vdW	simplified	43

^aNumbers in the parentheses are the U_{eff} in eV.

$$\eta = \max[(\Delta G_1 - 1.23 \text{ eV}), (\Delta G_2 - 1.23 \text{ eV}), \dots]/e$$

where ΔG_n is the free energy change of the n th elemental reaction in the OER, and e is the elementary charge. It should be noticed that the CHE model only counts the thermodynamics of intermediate states but omits the kinetics between them. The kinetics is certainly not unimportant. For example, it is known that the OER activity goes higher as pH increases,^{2,73} which, however, cannot be simply explained by the thermodynamic overpotential that is independent of pH.⁷⁴ By fitting to experimental data, Govind Rajan et al. developed a microkinetic model using the Marcus theory parameters to account for the electron transfer dynamics. The OER current density at different electrode potentials was thus correlated with pH values ranging from 13.0 to 14.7,⁷⁵ which rationalizes the dependence of the kinetics of electron transfer on the concentration of H⁺(aq).

In the DFT simulation of the OER on NiOOH, Li and Selloni first evaluated the OER activity on β -NiOOH (01 $\bar{1}$ 5) and γ -NiOOH (01 $\bar{1}$ 5) surfaces with PBE+U functional. They show that the OER on both surfaces follows the “lattice peroxide” path, where the *O_{latt}-O species is the key intermediate. The calculated thermodynamic overpotentials are 0.46 and 0.52 V for β -NiOOH and γ -NiOOH, respectively.¹⁶

Cater et al. modeled various active sites on the three most abundant facets of pristine β -NiOOH, the (0001), (10 $\bar{1}$ 2), and ($\bar{1}$ 2 $\bar{1}$ 3) faces, by using PBE+U and ONIOM-HSE06 methods.^{37,64} They show that the lowest thermodynamic

overpotentials on these three facets are comparable, 0.43–0.48 V, suggesting all of the low-index facets may attribute to the experimentally observed OER activity.

Goddard et al. investigated the OER on γ -NiOOH (01 $\bar{1}$ 2) by combining B3PW91 and implicit solvation model CANDLE.⁵⁰ They reported a high thermodynamic overpotential of 1.21 V follows the “electrochemical metal peroxide” path. The potential-determining step (PDS) is the O–O coupling step between the *O adatom and a H₂O molecule, with a kinetic barrier of 0.48 eV.

Table 2 reviews the mechanisms and the thermodynamic overpotentials for the OER on pure NiOOH reported in recent literature. For β -NiOOH, the OER activities on the (0001), (01 $\bar{1}$ 2), (01 $\bar{1}$ 0), and ($\bar{1}$ 2 $\bar{1}$ 1) faces have been studied, while for γ -NiOOH, the (01 $\bar{1}$ 0) and (01 $\bar{1}$ 2) faces have been investigated. The DFT calculations show that the thermodynamic overpotentials are in the range of 0.44–0.69 V on β -NiOOH (0001), 0.43–0.64 eV on (01 $\bar{1}$ 2), 0.28–0.93 V on (01 $\bar{1}$ 2), and 0.48–0.80 V on ($\bar{1}$ 2 $\bar{1}$ 3), while for γ -NiOOH, the thermodynamic overpotentials are 0.67 V on (01 $\bar{1}$ 0), 0.56–1.21 V on (01 $\bar{1}$ 2), and 0.52 V on (01 $\bar{1}$ 5). For comparison, the experimental overpotential of pure NiOOH is 0.53–0.60 V @ 10 mA/cm².²

From Table 2, one can be surprised that the reported thermodynamic overpotentials could be widely different: in the extreme case, the thermodynamic overpotential differs by up to 0.65 eV. The uncertainty of calculated thermodynamic overpotential could be attributed to a number of contributions:

(i) The inconsistent computational models for NiOOH.

Because the crystal structure of NiOOH remains unclear

in experiment, the structure models applied in various studies can be notably different.

- (ii) The different choice of calculation methods. As shown in Table 2, at least seven functionals, four Hubbard U values, and two solvation models were applied in the literature. The different setups can, to some extent, influence the reaction pathways and thermodynamic overpotentials.
- (V) The rich variation in the preferred mechanistic pathways of the OER. Given the NiOOH surface is hydroxylated, there are numerous possibilities for the sequence in the proton releasing. Therefore, the mechanisms derived by manual enumeration may well be incomplete, which then leads to different answer in energetics.

To underscore the complexity in characterizing the precise operative mechanism for the OER, Govind and Carter recently formulated an optimization framework to automatically enumerate OER pathways.⁶⁷ This framework uses the free energies of the various intermediates adsorbed on the catalyst surface as input and solves the OER pathways based on the mixed-integer linear programming. Figure 5 depicts all six OER

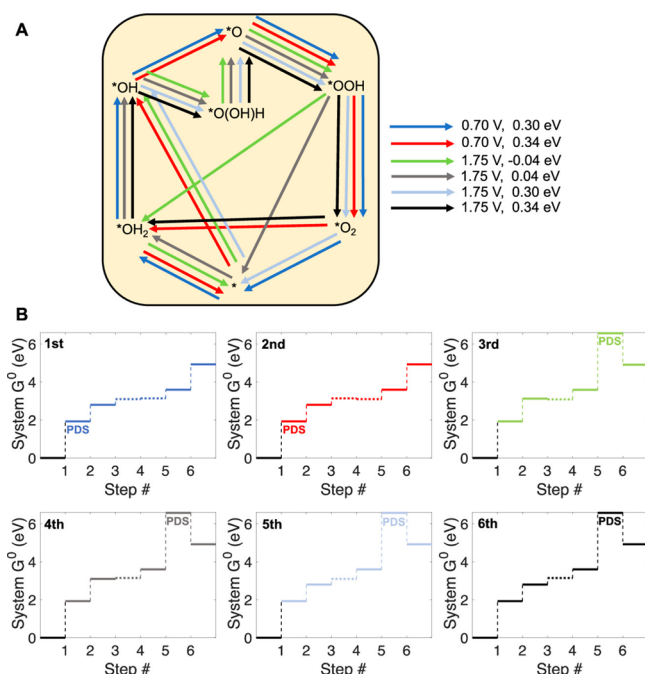


Figure 5. (A) Schematic of six automatically enumerated OER mechanisms discovered on β -NiOOH (0001). The corresponding thermodynamic overpotentials (V) and the highest nonelectroactive Gibbs free energy steps (eV) are indicated. (B) Energetic profiles for six mechanisms by PBE+U ($U_{\text{eff}} = 5.5$ eV). Reprinted from ref 67. Copyright 2020 American Chemical Society.

mechanisms discovered on the β -NiOOH (0001) surface with PBE+U functional. The best pathway, $* \rightarrow *OH_2 \rightarrow *OH \rightarrow *O \rightarrow *OOH \rightarrow *O_2 \rightarrow *$, follows the “water nucleophilic attack” path” and has a thermodynamic overpotential of $\eta = 0.70$ V, agreeing with the result in the previous literature.³⁷

4.2. OER on Defective NiOOH. Similar to all catalysis phenomena, the role of defects must be addressed in order to fully understand the kinetics. NiOOH material can have Ni vacancy, O vacancy, and OH vacancy depending on the reaction conditions. According to the Pourbaix diagram, Ni

vacancies exist on the surface at low-pH conditions, which will directly affect the OER activity by regulating the chemical environment of the active sites. In contrast, the O and OH vacancies are not favorable on the surface since they can be quickly healed by the dissociation of H_2O molecules. As a result, the O and OH vacancies are expected to be only available in the bulk and indirectly affect the OER activity by regulating the band structure.

The Ni vacancy appears to be critical for the unusual OER activity of NiOOH under neutral pH conditions. The conventional NiOOH catalyst can be stable and active only under a strong alkaline condition $pH \sim 14$,^{2,73} which makes it difficult to couple with reactions that achieves the highest activity only under neutral or acidic conditions.^{80–82} Recently, Bediako et al.⁸³ reported the electrodeposited NiOOH obtained from $Ni^{2+}(aq)$ solution containing borate electrolyte (denoted as NiB_i) can be a good OER catalyst down to the near-neutral pH (7–9).^{83–85} NiB_i is different from the conventional NiOOH in two aspects: the so-called “self-healing” ability of NiB_i, where the $Ni^{2+}(aq)$, if dissolved, can redeposit onto NiOOH surface dynamically with the assistance of borate,^{86,73} and the smaller particle size of NiB_i (2 nm vs 10 nm in the conventional NiOOH).^{84,85,87–89}

To clarify the origin of enhanced OER activity on NiB_i, our group studied thermodynamics for Ni dissolution from the γ -NiOOH (01 $\bar{1}$ 2) and the OER activity on the defective surface.⁴² Our results show that the dissolution of Ni vacancies occurs most at the surface Ni sites, with a free energy change of 0.09 eV. We then estimated around 4.3% of surface Ni ions are dissolved into the solution. Mechanistic studies show that the Ni^{4c} sites near the Ni vacancy can decrease the thermodynamic overpotential from 0.81 to 0.43 V.⁴²

By correlating the Ni^{4c} concentrations with the size of γ -NiOOH particles, we discovered that sub-10 nm γ -NiOOH particles can provide a significant number of Ni vacancies on the surface at the neutral pH condition. Figure 6 illustrates the

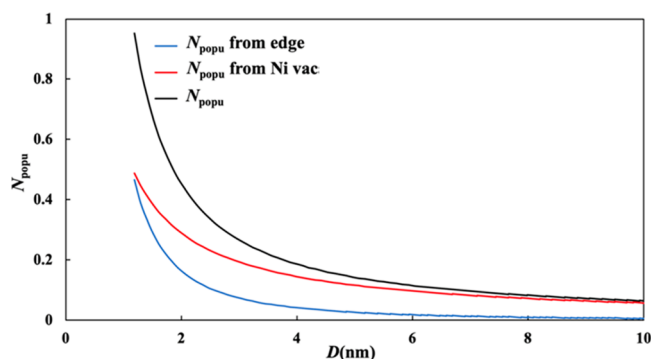


Figure 6. Population of Ni^{4c} vs γ -NiOOH particle size D . The black line is the overall population of Ni (N_{popu}) defined as $N_{\text{popu}} = Ni^{4c}/Ni^{\text{total}}$. The red line represents the N_{popu} contributed from the surface Ni vacancies; the blue line, the N_{popu} contributed from the edges. Reprinted from ref 42. Copyright 2020 American Chemical Society.

population of Ni^{4c} (N_{popu}) against the particle size grows from 1 to 10 nm. At 2 nm, the overall N_{popu} is around 0.44. As the size increases to 10 nm, N_{popu} diminishes to below 0.06. Therefore, we suggest that the unique OER activity of NiB_i in the neutral pH condition is mainly due to the small particle size of NiOOH.⁴²

As for the stability of O and OH vacancies, Toroker et al. reported that in the bulk β -NiOOH (with native structure) the formation of an OH vacancy is favorable in thermodynamics, while that of an O vacancy is not under O-rich and H-poor conditions (representing the high potential and high pH) by using PBE+U, PBE0, and HSE06 DFT functionals.⁹⁰ Their electronic structure analysis further identified shallow trapped states of OH vacancy.⁹⁰ Although the presence of OH vacancies on the surface is unlikely during the OER, Toroker et al. showed that the surface OH vacancy on β -NiOOH (01 $\bar{1}$ 5) can reduce the thermodynamic overpotential of the nearby Ni site from 0.61 to 0.26 V with the PBE+U functional. The reaction follows the “lattice peroxide” path, where the PDS is $*\text{H}_2\text{O} \rightarrow *\text{OH} + \text{H}^+(\text{aq}) + \text{e}^-$.⁹¹

4.3. OER on Fe-Doped NiOOH. For Fe-doped NiOOH, many theoretical calculations have agreed that the active site of the OER is the exposed Fe on the surface instead of the surrounding Ni,^{16,66,92} and the coordination environment of Fe can have a significant impact on its catalytic activity. On the bare NiOOH (0001), (01 $\bar{1}$ N) and ($\bar{1}$ 2 $\bar{1}$ N) surfaces, the Fe dopants are six-coordinated, five-coordinated, and four-coordinated, respectively. To reveal the role of Fe dopant, several groups have investigated the OER mechanism on various facets of Fe-doped NiOOH. For instance, Li and Selloni calculated the energetics of the OER on the Fe-doped β -NiOOH (01 $\bar{1}$ 5) and γ -NiOOH (01 $\bar{1}$ 5) with PBE+U functional.¹⁶ They showed that the OER on both Fe-doped surfaces follows the “lattice peroxide” path, with thermodynamic overpotentials of 0.26 and 0.48 V for β - and γ -NiOOH (cf. 0.46 and 0.52 for pure β - and γ -NiOOH in the same study).

Goddard et al. compared the OER activity between pure and Fe-doped γ -NiOOH (01 $\bar{1}$ 2) with B3PW91.⁵⁰ They showed that the thermodynamic overpotential decreases from 1.21 to 0.81 V after Fe doping. The OER on the Fe-doped surface follows the “electrochemical metal peroxide” path, where the O–O coupling is the PDS with a kinetic barrier of 0.64 eV.

Strasser et al. found a thermodynamic overpotential drop from 0.67 to 0.45 V when doping Fe on the γ -NiOOH (01 $\bar{1}$ 0) surface with optPBE+U.⁵² The reaction on the Fe-doped surface follows the “water nucleophilic attack” path, where the PDS is the deprotonation of $*\text{O}_{\text{lat}}\text{H}$.

Carter et al. reported the Fe doping on β -NiOOH ($\bar{1}$ 2 $\bar{1}$ 3) reduces the thermodynamic overpotential from 0.48 to 0.13 V by using HSE06 with $\alpha = 0.15$,⁶⁴ which is the lowest thermodynamic overpotential on Fe-doped NiOOH in the literature. Their results show that the OER follows the “lattice peroxide” path, while the formation of Fe-oxo species ($*\text{Fe}-\text{OH} \rightarrow *\text{Fe}=\text{O} + \text{H}^+(\text{aq}) + \text{e}^-$) is the PDS. They also showed that for the β -NiOOH (0001) surface, the surface Fe dopant only slightly reduces the thermodynamic overpotential (from 0.57 to 0.50 V) by using PBE+U.

By comparing the OER activity between the pure and Fe-doped β -NiOOH, Carter et al. proposed that the robust activity of the Fe-doped β -NiOOH is a combination of the ability of surface Fe^{3+} to stabilize the terminal oxo species ($*\text{Fe}^{4+}=\text{O}$) and the favorable discharge of adjacent Ni^{3+} to Ni^{2+} .⁶⁴ For comparison, the pure β -NiOOH tends to produce an unfavorable terminal oxyl radical ($\text{Ni}^{3+}-\text{O}^*$),⁶⁴ while on pure Fe oxides the discharge from Fe^{3+} to Fe^{2+} is difficult under OER conditions, although it can stabilize the terminal oxo. As result, both pure β -NiOOH and Fe oxides are poor OER electrocatalysts. Based on the above theory, Carter et al.

assess the OER mechanism and energetics when alternatively doping the β -NiOOH ($\bar{1}$ 2 $\bar{1}$ 3) surface with other transition metals, namely, V, Cr, Mn, Co, Mo, Ru, and Rh. They predicted Co is a competitive alternative to Fe, with only 0.07 V higher thermodynamic overpotential.⁹³

It is worth pointing out the remaining inconsistency between theory and experiment. The thermodynamic overpotential of Fe-doped β -NiOOH is calculated to be lower than that of Fe-doped γ -NiOOH. Specifically, the thermodynamic overpotential is down to 0.13 V,⁶⁴ while for γ -NiOOH it is at least 0.45 V.⁵² However, many experimental results suggested that γ -NiOOH is the active phase of the OER on Fe-doped NiOOH.⁴⁴ One possible cause for this inconsistency is the difficulty to synthesize the metastable pure β -NiOOH in experiment and thus the direct comparison of activity in experiment is not feasible. We note that pure β -NiOOH was recently synthesized by the epitaxial growth of NiOOH on the NiO matrix, which does exhibit a high OER activity.⁴⁵ More benchmarking work in experiment for Fe-doped β -NiOOH sample are needed in the field.

4.4. Important Issues in Computing the OER Activity.

In addition to the DFT functional, the theoretical OER activity is known to be sensitive to the structure model, the pH condition, and the solvent model. For the importance of dopant to the OER activity, the dopant position in the structural model is an important factor in determining the OER activity. Vandichel et al. investigate the influence of Fe dopant position on the different lattice sites of NiOOH with an explicit solvation model.⁴³ Their results show that the thermodynamic overpotential on the γ -NiOOH (01 $\bar{1}$ 2) surface with subsurface Fe dopant is 0.14 V, which is only one-sixth of that with surface Fe dopant (vs 0.84 V). In another study by Zhou et al., the thermodynamic overpotential of an intercalated Fe dopant is calculated to be 0.23 V.⁷⁷

Without question, the pH value can directly affect the OER activity, which is evidenced by the fact that NiOOH catalysts are generally limited at the alkaline condition. Govind Rajan et al. have shown that the concentration of $\text{H}^+(\text{aq})$ can affect directly the rate of the OER from Marcus theory.⁷⁵ More intricately, as also discussed in section 3.2 (see eq 3), the most stable structure of NiOOH electrodes may vary at different pH values according to the Pourbaix diagram. Huang and Zhou independently constructed a Pourbaix diagram for the Ni–H₂O system using HSE06 calculations.^{77,94} Both results show that the phase boundary of $\text{Ni}(\text{OH})_2/\text{NiOOH}$ locates, interestingly, at the typical potential that drives the OER (i.e., 1.5 V), indicating both phases may exist under the reaction conditions. The Fe doping may change the energy preference of different phases: Zhou et al. shows that in the Fe-doped Ni–H₂O system with a Fe concentration (Ni:Fe) of 1:23 the phase boundary of $\text{Ni}(\text{OH})_2/\text{NiOOH}$ moves toward the low electrode potential end compared to the undoped one, indicating the NiOOH phase becomes more favorable after Fe doping.⁷⁷

5. OUTLOOK

While tremendous progresses has been made in recent years in understanding the NiOOH structure and catalysis, many more challenges are identified and need to be solved by theory in the future. It is now well established that the working NiOOH catalysts deviate from the formal oxidation of Ni^{3+} , but being a mixture of Ni^{3+} and Ni^{4+} . The exact ratio of Ni^{3+} and Ni^{4+} depends on the synthetic conditions and thus vary from phase

to phase. The complex PES of NiOOH lies not only in many possible structure candidates but also in the complex electronic structures and the solvent effect of the electrolyte. These have led to the great uncertainty on the active sites of NiOOH catalysts.

For the NiOOH structures, most studies focus on the variety of the intercalated species, in particular, the amount and configurations of the intercalated species that determine the Ni oxidation state and the interlayer spacing of the NiO₂ framework, while the NiO₂ framework is generally believed to be layered. However, the discovery of tunneled NiOOH suggests that there may be new NiO₂ frameworks that have not been considered yet. This new finding motivates us to explore new structure candidates for NiOOH. By using the new technique, i.e., machine learning global PES optimization, we screen the bulk crystal structure candidates of β -NiOOH with H concentrations (H:Ni) from 0 to 2. We observed a series of new structures once the H concentration is below 0.5, where local O–O peroxide bonding appears in a tunneled NiO₂ framework. More studies are required to validate and unify the current NiOOH bulk and surface models.

Besides the atomic arrangement, the O concentration (O:Ni) in the NiO₂ framework may also change during reactions. For instance, in the “lattice peroxide” and the “water nucleophilic attack” paths of the OER, the intermediate O atoms (oxidated from water molecules) can insert into the NiO₂ framework by forming lattice O–O peroxide. This process may increase the O concentration of the NiO₂ framework, i.e., NiOOH \rightarrow NiO_{2+x}H, thereby changing the NiOOH structure. This possibility, however, has not been discussed in the literature. In fact, one structural analogue known as nickel peroxide (NiO_{2+x}H_y) has already been synthesized by the chemical oxidation of Ni(OH)₂ using strong oxidants, such as O₃, NaClO, or Na₂S₂O₈.^{95–97} The operative conditions of the OER are also a strong oxidated environment similar to that of chemical oxidants. So, the NiO_{2+x}H may also appear in the OER process, and its structure and stability should also be examined in future studies.

For the electronic structures of NiOOH, current DFT functionals, such as DFT+U, DFT-vdW, and even hybrid functionals, cannot provide satisfied accuracy for both energetics and band structures. At the moment, DFT+U calculations are still expected to be the most available tool for optimizing structure and identifying the local oxidation state, due to its low computational cost. The post-DFT methods such as hybrid HSE06, although it is highly computationally demanding, are required to verify the conclusions from DFT+U, in particular those related to band structures. Further progress in the electronic structure calculations in treating the strongly correlated systems will be most welcome for benchmarking and computing the energetics of NiOOH phases. For instance, in the DFT approach, the double-hybrid functional can provide improved energetics and electronic structures for both main group elements and transition metals. However, this functional has rarely been applied in the periodic system due to the inherent computational complexity. Recently, well-converged periodic calculations with the double-hybrid functional have been achieved,⁹⁸ this advance may promote the simulations of NiOOH with these higher-level functionals. In the wave function approach, the embedded correlated wave function theory has been applied to investigate the heterogeneous catalysis, where the active site on the catalyst's surface is described by the highly accurate wave

function method, such as CASSCF/CASPT2.⁹⁹ Although these new methods are still expensive and have a few technical difficulties, their application to NiOOH is valuable, which can provide a reliable reference for other DFT functionals.

The high current density and low overpotential are always the central goals to achieve for designing applicable electrochemical catalysts. For this purpose, the kinetics in the oxygen evolution reaction, in particular those related to Tafel slope, should be resolved. For this purpose, we need to evaluate the kinetics of electron transfer in electrochemical reactions. According to Marcus theory, the rate of electron transfer is determined by the reorganization energy. This parameter is not directly determined by geometrical parameters, such as bond length, bond angle, and dihedral angle, but is related to the excited state of the system. Therefore, the reorganization energy cannot be calculated by standard DFT methods. Instead, a constrained DFT that can force the electron in a specific site should be applied. Overall, the study of electron transfer on NiOOH is still scarce, we expect to see the advance on this topic in the future.

Aside from the electrode material, the electrolyte is also important for the stability of NiOOH. The electrolyte involves solvated ions, such as phosphate, borate anions, Na⁺, and, K⁺ cations. To clarify the effects of these ions, one should simulate the NiOOH/electrolyte interface by combining the explicit solvation model and MD simulations, which is, however, very expensive for first-principles calculations. Fortunately, recently developed machine learning PES can significantly boost the speed of MD simulations, making the simulation of electrolyte on the NiOOH surface available.

The coming years might witness a boom in theoretical simulations of NiOOH in the more realistic environment, e.g., including the NiOOH surfaces, the explicit solution, and the electrolyte. These exciting developments could benefit from machine learning based atomic simulation.

■ ASSOCIATED CONTENT

SI Supporting Information

The Supporting Information is available free of charge at <https://pubs.acs.org/doi/10.1021/acs.jpcc.1c06170>.

Correspondence between two sets of Miller–Bravais indices (PDF)

■ AUTHOR INFORMATION

Corresponding Authors

Ye-Fei Li – Collaborative Innovation Center of Chemistry for Energy Material, Key Laboratory of Computational Physical Science (Ministry of Education), Shanghai Key Laboratory of Molecular Catalysis and Innovative Materials, Department of Chemistry, Fudan University, Shanghai 200433, China; Email: yefeil@fudan.edu.cn

Zhi-Pan Liu – Collaborative Innovation Center of Chemistry for Energy Material, Key Laboratory of Computational Physical Science (Ministry of Education), Shanghai Key Laboratory of Molecular Catalysis and Innovative Materials, Department of Chemistry, Fudan University, Shanghai 200433, China; orcid.org/0000-0002-2906-5217; Email: zpliu@fudan.edu.cn

Author

Ji-Li Li – Collaborative Innovation Center of Chemistry for Energy Material, Key Laboratory of Computational Physical

Science (Ministry of Education), Shanghai Key Laboratory of Molecular Catalysis and Innovative Materials, Department of Chemistry, Fudan University, Shanghai 200433, China

Complete contact information is available at:
<https://pubs.acs.org/10.1021/acs.jpcc.1c06170>

Notes

The authors declare no competing financial interest.

Biographies

Ye-Fei Li is a full Professor at Fudan University (Shanghai, PR China). Prior to joining the faculty at Fudan in 2014, he was a postdoctoral fellow in the Department of Chemistry at Princeton University. He received his Ph.D. degree from Fudan University in 2012. His current research interests are mainly focused on metal oxide materials, surfaces, interfaces, photo/electrocatalysis, and photo-voltaics.

Ji-Li Li received her B.S. from East China University of Science and Technology in 2019. She is now a Ph.D. candidate in Department of Chemistry at Fudan University. Her current research interests are first-principles reaction dynamics of heterogeneous catalysis.

Zhipan Liu received his B.S. from Shanghai Jiaotong University in 1997 and his Ph.D. from Queen's University of Belfast (U.K.) in 2003. He was a postdoctoral associate at University of Cambridge (U.K.) from 2003 to 2005 and a full professor in Department of Chemistry at Fudan University from 2005. His current research interests include (i) heterogeneous catalysis, (ii) global optimization and pathway search, and (iii) machine learning potential methods and simulation.

ACKNOWLEDGMENTS

This work was supported by the National Key Research and Development Program of China (2018YFA0208600) and the National Science Foundation of China (21773032, 21972023, 21533001, 91545107, 91745201).

REFERENCES

- (1) Gong, M.; Li, Y.; Wang, H.; Liang, Y.; Wu, J. Z.; Zhou, J.; Wang, J.; Regier, T.; Wei, F.; Dai, H. An Advanced Ni–Fe Layered Double Hydroxide Electrocatalyst for Water Oxidation. *J. Am. Chem. Soc.* **2013**, *135*, 8452–8455.
- (2) Klaus, S.; Cai, Y.; Louie, M. W.; Trotochaud, L.; Bell, A. T. Effects of Fe Electrolyte Impurities on Ni(OH)₂/NiOOH Structure and Oxygen Evolution Activity. *J. Phys. Chem. C* **2015**, *119*, 7243–7254.
- (3) Bender, M. T.; Lam, Y. C.; Hammes-Schiffer, S.; Choi, K.-S. Unraveling Two Pathways for Electrochemical Alcohol and Aldehyde Oxidation on NiOOH. *J. Am. Chem. Soc.* **2020**, *142*, 21538–21547.
- (4) Lu, S.; Hummel, M.; Gu, Z.; Wang, Y.; Wang, K.; Pathak, R.; Zhou, Y.; Jia, H.; Qi, X.; Zhao, X.; et al. Highly Efficient Urea Oxidation via Nesting Nano-Nickel Oxide in Eggshell Membrane-Derived Carbon. *ACS Sustainable Chem. Eng.* **2021**, *9*, 1703–1713.
- (5) Li, Y.; Jiang, H.; Cui, Z.; Zhu, S.; Li, Z.; Wu, S.; Ma, L.; Han, X.; Liang, Y. Spin State Tuning of the Octahedral Sites in Ni–Co-Based Spinel toward Highly Efficient Urea Oxidation Reaction. *J. Phys. Chem. C* **2021**, *125*, 9190–9199.
- (6) Louie, M. W.; Bell, A. T. An Investigation of Thin-Film Ni–Fe Oxide Catalysts for the Electrochemical Evolution of Oxygen. *J. Am. Chem. Soc.* **2013**, *135*, 12329–12337.
- (7) Casas-Cabanas, M.; Canales-Vázquez, J.; Rodríguez-Carvajal, J.; Palacín, M. R. Deciphering the Structural Transformations during Nickel Oxyhydroxide Electrode Operation. *J. Am. Chem. Soc.* **2007**, *129*, 5840–5842.
- (8) Jugner, W. Verfahren zur Elektrolytischen Vergrößerung der Oberfläche von Masseträgern aus Eisen, Nickel oder Kobalt für Elektroden in alkalischen Sammlern. German Patent 163 170 1901.
- (9) Jugner, W. Elektrischen Sammlern mit unveränderlichem alkalischen Elektrolyten. German Patent 157 290 1901.
- (10) Edison, T. A. Reversible galvanic battery. US692507A 1901.
- (11) Barnard, R.; Randell, C. F.; Tye, F. L. Studies concerning charged nickel hydroxide electrodes I. Measurement of reversible potentials. *J. Appl. Electrochem.* **1980**, *10*, 109–125.
- (12) Klápště, B.; Micka, K.; Mrha, J.; Vondrák, J. Plastic-bonded electrodes for nickel–cadmium accumulators. X. The nature of the second discharge step of nickel oxide electrodes. *J. Power Sources* **1982**, *8*, 351–357.
- (13) Briggs, G. W. D.; Jones, E.; Wynne-Jones, W. F. K. The nickel oxide electrode. Part 1. *Trans. Faraday Soc.* **1955**, *51*, 1433–1442.
- (14) Bode, H.; Dehmelt, K.; Witte, J. Zur kenntnis der nickel-hydroxidelektrode—I. Über das nickel (II)-hydroxidhydrat. *Electrochim. Acta* **1966**, *11*, 1079–1087.
- (15) Oliva, P.; Leonardi, J.; Laurent, J. F.; Delmas, C.; Braconnier, J. J.; Figlarz, M.; Fievet, F.; Guibert, A. d. Review of the structure and the electrochemistry of nickel hydroxides and oxy-hydroxides. *J. Power Sources* **1982**, *8*, 229–255.
- (16) Li, Y.-F.; Selloni, A. Mechanism and Activity of Water Oxidation on Selected Surfaces of Pure and Fe-Doped NiO_x. *ACS Catal.* **2014**, *4*, 1148–1153.
- (17) Dou, Y.; He, C.-T.; Zhang, L.; Al-Mamun, M.; Guo, H.; Zhang, W.; Xia, Q.; Xu, J.; Jiang, L.; Wang, Y.; Liu, P.; Chen, X.-M.; Yin, H.; Zhao, H. How Cobalt and Iron Doping Determine the Oxygen Evolution Electrocatalytic Activity of NiOOH. *Cell Rep. Phys. Sci.* **2020**, *1*, 100077.
- (18) Wang, A.-L.; Xu, H.; Li, G.-R. NiCoFe Layered Triple Hydroxides with Porous Structures as High-Performance Electrocatalysts for Overall Water Splitting. *ACS Energy Lett.* **2016**, *1*, 445–453.
- (19) Detsi, E.; Cook, J. B.; Lesel, B. K.; Turner, C. L.; Liang, Y.-L.; Robbenolt, S.; Tolbert, S. H. Mesoporous Ni₆₀Fe₃₀Mn₁₀-alloy based metal/metal oxide composite thick films as highly active and robust oxygen evolution catalysts. *Energy Environ. Sci.* **2016**, *9*, 540–549.
- (20) Liu, J.; Cheng, W.; Tang, F.; Su, H.; Huang, Y.; Hu, F.; Zhao, X.; Jiang, Y.; Liu, Q.; Wei, S. Electron Delocalization Boosting Highly Efficient Electrocatalytic Water Oxidation in Layered Hydroxalicates. *J. Phys. Chem. C* **2017**, *121*, 21962–21968.
- (21) Liu, H.; Wang, Y.; Lu, X.; Hu, Y.; Zhu, G.; Chen, R.; Ma, L.; Zhu, H.; Tie, Z.; Liu, J. The effects of Al substitution and partial dissolution on ultrathin NiFeAl ternary layered double hydroxide nanosheets for oxygen evolution reaction in alkaline solution. *Nano Energy* **2017**, *35*, 350–357.
- (22) Casey, E. J.; Dubois, A. R.; Lake, P. E.; Moroz, W. J. Effects of Foreign Ions on Nickel Hydroxide and Cadmium Electrodes. *J. Electrochem. Soc.* **1965**, *112*, 371.
- (23) Corrigan, D. A.; Bendert, R. M. Effect of Coprecipitated Metal Ions on the Electrochemistry of Nickel Hydroxide Thin Films: Cyclic Voltammetry in 1M KOH. *J. Electrochem. Soc.* **1989**, *136*, 723–728.
- (24) Corrigan, D. A. The Catalysis of the Oxygen Evolution Reaction by Iron Impurities in Thin Film Nickel Oxide Electrodes. *J. Electrochem. Soc.* **1987**, *134*, 377–384.
- (25) Miller, E. L.; Rocheleau, R. E. Electrochemical Behavior of Reactively Sputtered Iron-Doped Nickel Oxide. *J. Electrochem. Soc.* **1997**, *144*, 3072–3077.
- (26) Młynarek, G.; Paszkiewicz, M.; Radniecka, A. The effect of ferric ions on the behaviour of a nickelous hydroxide electrode. *J. Appl. Electrochem.* **1984**, *14*, 145–149.
- (27) Hohenberg, P.; Kohn, W. Inhomogeneous Electron Gas. *Phys. Rev.* **1964**, *136*, B864–B871.
- (28) Kohn, W.; Sham, L. J. Self-Consistent Equations Including Exchange and Correlation Effects. *Phys. Rev.* **1965**, *140*, A1133–A1138.

- (29) Perdew, J. P.; Burke, K.; Ernzerhof, M. Generalized Gradient Approximation Made Simple. *Phys. Rev. Lett.* **1996**, *77*, 3865–3868.
- (30) Mori-Sánchez, P.; Cohen, A. J.; Yang, W. Localization and Delocalization Errors in Density Functional Theory and Implications for Band-Gap Prediction. *Phys. Rev. Lett.* **2008**, *100*, 146401.
- (31) Anisimov, V. I.; Zaanen, J.; Andersen, O. K. Band theory and Mott insulators: Hubbard U instead of Stoner I. *Phys. Rev. B: Condens. Matter Mater. Phys.* **1991**, *44*, 943–954.
- (32) Adamo, C.; Barone, V. Toward reliable density functional methods without adjustable parameters: The PBE0 model. *J. Chem. Phys.* **1999**, *110*, 6158–6170.
- (33) Heyd, J.; Scuseria, G. E.; Ernzerhof, M. Hybrid functionals based on a screened Coulomb potential. *J. Chem. Phys.* **2003**, *118*, 8207–8215.
- (34) Dudarev, S. L.; Botton, G. A.; Savrasov, S. Y.; Humphreys, C. J.; Sutton, A. P. Electron-energy-loss spectra and the structural stability of nickel oxide: An LSDA+U study. *Phys. Rev. B: Condens. Matter Mater. Phys.* **1998**, *57*, 1505–1509.
- (35) Li, Y.-F.; Liu, Z.-P. Structure and water oxidation activity of 3d metal oxides. *Wiley Interdiscip. Rev. Comput. Mol. Sci.* **2016**, *6*, 47–64.
- (36) Meng, Y.; Liu, X.-W.; Huo, C.-F.; Guo, W.-P.; Cao, D.-B.; Peng, Q.; Dearden, A.; Gonze, X.; Yang, Y.; Wang, J.; Jiao, H.; Li, Y.; Wen, X.-D. When Density Functional Approximations Meet Iron Oxides. *J. Chem. Theory Comput.* **2016**, *12*, 5132–5144.
- (37) Govind Rajan, A.; Martinez, J. M. P.; Carter, E. A. Facet-Independent Oxygen Evolution Activity of Pure β -NiOOH: Different Chemistries Leading to Similar Overpotentials. *J. Am. Chem. Soc.* **2020**, *142*, 3600–3612.
- (38) Li, Y.-F.; Liu, Z.-P.; Liu, L.; Gao, W. Mechanism and Activity of Photocatalytic Oxygen Evolution on Titania Anatase in Aqueous Surroundings. *J. Am. Chem. Soc.* **2010**, *132*, 13008–13015.
- (39) Fattebert, J.-L.; Gygi, F. Density functional theory for efficient ab initio molecular dynamics simulations in solution. *J. Comput. Chem.* **2002**, *23*, 662–666.
- (40) Fattebert, J. L.; Gygi, F. Linear-scaling first-principles molecular dynamics with plane-waves accuracy. *Phys. Rev. B: Condens. Matter Mater. Phys.* **2006**, *73*, 115124.
- (41) Fattebert, J.-L.; Gygi, F. First-principles molecular dynamics simulations in a continuum solvent. *Int. J. Quantum Chem.* **2003**, *93*, 139–147.
- (42) Li, L.-F.; Li, Y.-F.; Liu, Z.-P. Oxygen Evolution Activity on NiOOH Catalysts: Four-Coordinated Ni Cation as the Active Site and the Hydroperoxide Mechanism. *ACS Catal.* **2020**, *10*, 2581–2590.
- (43) Vandichel, M.; Busch, M.; Laasonen, K. Oxygen Evolution on Metal-oxy-hydroxides: Beneficial Role of Mixing Fe, Co, Ni Explained via Bifunctional Edge/acceptor Route. *ChemCatChem* **2020**, *12*, 1436–1442.
- (44) Friebel, D.; Louie, M. W.; Bajdich, M.; Sanwald, K. E.; Cai, Y.; Wise, A. M.; Cheng, M.-J.; Sokaras, D.; Weng, T.-C.; Alonso-Mori, R.; Davis, R. C.; Bargar, J. R.; Nørskov, J. K.; Nilsson, A.; Bell, A. T. Identification of Highly Active Fe Sites in (Ni,Fe)OOH for Electrocatalytic Water Splitting. *J. Am. Chem. Soc.* **2015**, *137*, 1305–1313.
- (45) Kim, B.; Oh, A.; Kabiraz, M. K.; Hong, Y.; Joo, J.; Baik, H.; Choi, S.-I.; Lee, K. NiOOH Exfoliation-Free Nickel Octahedra as Highly Active and Durable Electrocatalysts Toward the Oxygen Evolution Reaction in an Alkaline Electrolyte. *ACS Appl. Mater. Interfaces* **2018**, *10*, 10115–10122.
- (46) Delahaye-Vidal, A.; Beaudoin, B.; Figlarz, M. Textural and structural studies on nickel hydroxide electrodes: I. Crystallized nickel hydroxide materials submitted to chemical and electrochemical redox cycling. *React. Solids* **1986**, *2*, 223–233.
- (47) Martinez, J. M. P.; Carter, E. A. Effects of the Aqueous Environment on the Stability and Chemistry of β -NiOOH Surfaces. *Chem. Mater.* **2018**, *30*, 5205–5219.
- (48) Li, Y.-F.; Selloni, A. Mosaic Texture and Double c-Axis Periodicity of β -NiOOH: Insights from First-Principles and Genetic Algorithm Calculations. *J. Phys. Chem. Lett.* **2014**, *5*, 3981–3985.
- (49) Shin, H.; Xiao, H.; Goddard, W. A. In Silico Discovery of New Dopants for Fe-Doped Ni Oxyhydroxide (Ni_{1-x}Fe_xOOH) Catalysts for Oxygen Evolution Reaction. *J. Am. Chem. Soc.* **2018**, *140*, 6745–6748.
- (50) Xiao, H.; Shin, H.; Goddard, W. A. Synergy between Fe and Ni in the optimal performance of (Ni,Fe)OOH catalysts for the oxygen evolution reaction. *Proc. Natl. Acad. Sci. U. S. A.* **2018**, *115*, 5872.
- (51) Yang, X.; Takada, K.; Itose, M.; Ebina, Y.; Ma, R.; Fukuda, K.; Sasaki, T. Highly Swollen Layered Nickel Oxide with a Trilayer Hydrate Structure. *Chem. Mater.* **2008**, *20*, 479–485.
- (52) Dionigi, F.; Zeng, Z.; Sinev, I.; Merzdorf, T.; Deshpande, S.; Lopez, M. B.; Kunze, S.; Zegkinoglou, I.; Sarodnik, H.; Fan, D.; Bergmann, A.; Drnec, J.; Araujo, J. F. d.; Gliech, M.; Teschner, D.; Zhu, J.; Li, W.-X.; Greeley, J.; Cuenya, B. R.; Strasser, P. In-situ structure and catalytic mechanism of NiFe and CoFe layered double hydroxides during oxygen evolution. *Nat. Commun.* **2020**, *11*, 2522.
- (53) Liu, X.; Ni, K.; Wen, B.; Guo, R.; Niu, C.; Meng, J.; Li, Q.; Wu, P.; Zhu, Y.; Wu, X.; Mai, L. Deep Reconstruction of Nickel-Based Precatalysts for Water Oxidation Catalysis. *ACS Energy Lett.* **2019**, *4*, 2585–2592.
- (54) Zhang, X.-J.; Shang, C.; Liu, Z.-P. Double-Ended Surface Walking Method for Pathway Building and Transition State Location of Complex Reactions. *J. Chem. Theory Comput.* **2013**, *9*, 5745–5753.
- (55) Zhang, X.-J.; Liu, Z.-P. Variable-Cell Double-Ended Surface Walking Method for Fast Transition State Location of Solid Phase Transitions. *J. Chem. Theory Comput.* **2015**, *11*, 4885–4894.
- (56) Huang, S.-D.; Shang, C.; Zhang, X.-J.; Liu, Z.-P. Material discovery by combining stochastic surface walking global optimization with a neural network. *Chem. Sci.* **2017**, *8*, 6327–6337.
- (57) Huang, S.-D.; Shang, C.; Kang, P.-L.; Liu, Z.-P. Atomic structure of boron resolved using machine learning and global sampling. *Chem. Sci.* **2018**, *9*, 8644.
- (58) Huang, S.-D.; Shang, C.; Kang, P.-L.; Zhang, X.-J.; Liu, Z.-P. LASP: Fast global potential energy surface exploration. *Wiley Interdiscip. Rev.: Comput. Mol. Sci.* **2019**, *9*, e1415.
- (59) Kang, P.-L.; Shang, C.; Liu, Z.-P. Glucose to 5-Hydroxymethylfurfural: Origin of Site-Selectivity Resolved by Machine Learning Based Reaction Sampling. *J. Am. Chem. Soc.* **2019**, *141*, 20525–20536.
- (60) Carpenter, M. K.; Corrigan, D. A. Photoelectrochemistry of Nickel Hydroxide Thin Films. *J. Electrochem. Soc.* **1989**, *136*, 1022–1026.
- (61) Biesinger, M. C.; Payne, B. P.; Lau, L. W. M.; Gerson, A.; Smart, R. S. C. X-ray photoelectron spectroscopic chemical state quantification of mixed nickel metal, oxide and hydroxide systems. *Surf. Interface Anal.* **2009**, *41*, 324–332.
- (62) Tkalych, A. J.; Yu, K.; Carter, E. A. Structural and Electronic Features of β -Ni(OH)₂ and β -NiOOH from First Principles. *J. Phys. Chem. C* **2015**, *119*, 24315–24322.
- (63) Zaffran, J.; Caspary Toroker, M. Benchmarking Density Functional Theory Based Methods To Model NiOOH Material Properties: Hubbard and van der Waals Corrections vs Hybrid Functionals. *J. Chem. Theory Comput.* **2016**, *12*, 3807–3812.
- (64) Martinez, J. M. P.; Carter, E. A. Unraveling Oxygen Evolution on Iron-Doped β -Nickel Oxyhydroxide: The Key Role of Highly Active Molecular-like Sites. *J. Am. Chem. Soc.* **2019**, *141*, 693–705.
- (65) Tkalych, A. J.; Zhuang, H. L.; Carter, E. A. A Density Functional + U Assessment of Oxygen Evolution Reaction Mechanisms on β -NiOOH. *ACS Catal.* **2017**, *7*, 5329–5339.
- (66) Tkalych, A. J.; Martinez, J. M. P.; Carter, E. A. Effect of transition-metal-ion dopants on the oxygen evolution reaction on NiOOH(0001). *Phys. Chem. Chem. Phys.* **2018**, *20*, 19525–19531.
- (67) Govind Rajan, A.; Carter, E. A. Discovering Competing Electrocatalytic Mechanisms and Their Overpotentials: Automated Enumeration of Oxygen Evolution Pathways. *J. Phys. Chem. C* **2020**, *124*, 24883–24898.
- (68) Kumar, M.; Piccinin, S.; Srinivasan, V. Direct and Indirect Role of Fe Doping in NiOOH Monolayer for Water Oxidation Catalysis. *ChemRxiv* **2021**, DOI: 10.33774/chemrxiv-2021-kthjg. This content is a preprint and has not been peer-reviewed.

- (69) Bajdich, M.; García-Mota, M.; Vojvodic, A.; Nørskov, J. K.; Bell, A. T. Theoretical Investigation of the Activity of Cobalt Oxides for the Electrochemical Oxidation of Water. *J. Am. Chem. Soc.* **2013**, *135*, 13521–13530.
- (70) García-Mota, M.; Vojvodic, A.; Metiu, H.; Man, I. C.; Su, H.-Y.; Rossmeis, J.; Nørskov, J. K. Tailoring the Activity for Oxygen Evolution Electrocatalysis on Rutile TiO₂(110) by Transition-Metal Substitution. *ChemCatChem* **2011**, *3*, 1607–1611.
- (71) Valdés, A.; Qu, Z. W.; Kroes, G. J.; Rossmeis, J.; Nørskov, J. K. Oxidation and Photo-Oxidation of Water on TiO₂ Surface. *J. Phys. Chem. C* **2008**, *112*, 9872–9879.
- (72) Li, Y.-F.; Liu, Z.-P. Active Site Revealed for Water Oxidation on Electrochemically Induced δ -MnO₂: Role of Spinel-to-Layer Phase Transition. *J. Am. Chem. Soc.* **2018**, *140*, 1783–1792.
- (73) Diaz-Morales, O.; Ferrus-Suspedra, D.; Koper, M. T. M. The importance of nickel oxyhydroxide deprotonation on its activity towards electrochemical water oxidation. *Chem. Sci.* **2016**, *7*, 2639–2645.
- (74) Chen, J.; Li, Y.-F.; Sit, P.; Selloni, A. Chemical Dynamics of the First Proton-Coupled Electron Transfer of Water Oxidation on TiO₂ Anatase. *J. Am. Chem. Soc.* **2013**, *135*, 18774–18777.
- (75) Govind Rajan, A.; Carter, E. A. Microkinetic model for pH- and potential-dependent oxygen evolution during water splitting on Fe-doped β -NiOOH. *Energy Environ. Sci.* **2020**, *13*, 4962–4976.
- (76) Hareli, C.; Casparly Toroker, M. Water Oxidation Catalysis for NiOOH by a Metropolis Monte Carlo Algorithm. *J. Chem. Theory Comput.* **2018**, *14*, 2380–2385.
- (77) Zhou, Y.; López, N. The Role of Fe Species on NiOOH in Oxygen Evolution Reactions. *ACS Catal.* **2020**, *10*, 6254–6261.
- (78) Costanzo, F. Effect of doping β -NiOOH with Co on the catalytic oxidation of water: DFT+U calculations. *Phys. Chem. Chem. Phys.* **2016**, *18*, 7490–7501.
- (79) Xue, Z.; Zhang, X.; Qin, J.; Liu, R. Revealing Ni-based layered double hydroxides as high-efficiency electrocatalysts for the oxygen evolution reaction: a DFT study. *J. Mater. Chem. A* **2019**, *7*, 23091–23097.
- (80) Popczun, E. J.; McKone, J. R.; Read, C. G.; Biacchi, A. J.; Wiltout, A. M.; Lewis, N. S.; Schaak, R. E. Nanostructured Nickel Phosphide as an Electrocatalyst for the Hydrogen Evolution Reaction. *J. Am. Chem. Soc.* **2013**, *135*, 9267–9270.
- (81) Saadi, F. H.; Carim, A. I.; Drisdell, W. S.; Gul, S.; Baricuatro, J. H.; Yano, J.; Soriaga, M. P.; Lewis, N. S. Operando Spectroscopic Analysis of CoP Films Electrocatalyzing the Hydrogen-Evolution Reaction. *J. Am. Chem. Soc.* **2017**, *139*, 12927–12930.
- (82) Li, Y.; Zhang, L. A.; Qin, Y.; Chu, F.; Kong, Y.; Tao, Y.; Li, Y.; Bu, Y.; Ding, D.; Liu, M. Crystallinity Dependence of Ruthenium Nanocatalyst toward Hydrogen Evolution Reaction. *ACS Catal.* **2018**, *8*, 5714–5720.
- (83) Bediako, D. K.; Surendranath, Y.; Nocera, D. G. Mechanistic studies of the oxygen evolution reaction mediated by a nickel–borate thin film electrocatalyst. *J. Am. Chem. Soc.* **2013**, *135*, 3662–3674.
- (84) Dincă, M.; Surendranath, Y.; Nocera, D. G. Nickel-borate oxygen-evolving catalyst that functions under benign conditions. *Proc. Natl. Acad. Sci. U. S. A.* **2010**, *107*, 10337.
- (85) Bediako, D. K.; Lassalle-Kaiser, B.; Surendranath, Y.; Yano, J.; Yachandra, V. K.; Nocera, D. G. Structure–Activity Correlations in a Nickel–Borate Oxygen Evolution Catalyst. *J. Am. Chem. Soc.* **2012**, *134*, 6801–6809.
- (86) Lutterman, D. A.; Surendranath, Y.; Nocera, D. G. A Self-Healing Oxygen-Evolving Catalyst. *J. Am. Chem. Soc.* **2009**, *131*, 3838–3839.
- (87) Risch, M.; Klingan, K.; Heidkamp, J.; Ehrenberg, D.; Chernev, P.; Zaharieva, I.; Dau, H. Nickel-oxido structure of a water-oxidizing catalyst film. *Chem. Commun.* **2011**, *47*, 11912–11914.
- (88) Yoshida, M.; Mitsutomi, Y.; Mineo, T.; Nagasaka, M.; Yuzawa, H.; Kosugi, N.; Kondoh, H. Direct Observation of Active Nickel Oxide Cluster in Nickel–Borate Electrocatalyst for Water Oxidation by In Situ O K-Edge X-ray Absorption Spectroscopy. *J. Phys. Chem. C* **2015**, *119*, 19279–19286.
- (89) Trotochaud, L.; Young, S. L.; Ranney, J. K.; Boettcher, S. W. Nickel–Iron Oxyhydroxide Oxygen-Evolution Electrocatalysts: The Role of Intentional and Incidental Iron Incorporation. *J. Am. Chem. Soc.* **2014**, *136*, 6744–6753.
- (90) Dhaka, K.; Toroker, M. C. Revealing the Conducting Character of the β -NiOOH Catalyst through Defect Chemistry. *J. Phys. Chem. C* **2019**, *123*, 18895–18904.
- (91) Fidelsky, V.; Toroker, M. C. Enhanced Water Oxidation Catalysis of Nickel Oxyhydroxide through the Addition of Vacancies. *J. Phys. Chem. C* **2016**, *120*, 25405–25410.
- (92) Bo, X.; Hocking, R. K.; Zhou, S.; Li, Y.; Chen, X.; Zhuang, J.; Du, Y.; Zhao, C. Capturing the active sites of multimetallic (oxy)hydroxides for the oxygen evolution reaction. *Energy Environ. Sci.* **2020**, *13*, 4225–4237.
- (93) Martinez, J. M. P.; Carter, E. A. Noninnocent Influence of Host β -NiOOH Redox Activity on Transition-Metal Dopants' Efficacy as Active Sites in Electrocatalytic Water Oxidation. *ACS Catal.* **2020**, *10*, 2720–2734.
- (94) Huang, L. F.; Hutchison, M. J.; Santucci, R. J.; Scully, J. R.; Rondinelli, J. M. Improved Electrochemical Phase Diagrams from Theory and Experiment: The Ni–Water System and Its Complex Compounds. *J. Phys. Chem. C* **2017**, *121*, 9782–9789.
- (95) Nakagawa, K.; Konaka, R.; Nakata, T. Oxidation with nickel peroxide. I. Oxidation of alcohols. *J. Org. Chem.* **1962**, *27*, 1597–1601.
- (96) Yang, W. L.; Yang, X. P.; Hou, C. M.; Li, B. J.; Gao, H. T.; Lin, J. H.; Luo, X. L. Rapid room-temperature fabrication of ultrathin Ni(OH)₂ nanoflakes with abundant edge sites for efficient urea oxidation. *Appl. Catal., B* **2019**, *259*, 118020.
- (97) Thendral, P.; Shailaja, S.; Ramachandran, M. Nickel peroxide: A more probable intermediate in the Ni (II)-catalyzed decomposition of peroxomonosulfate. *Int. J. Chem. Kinet.* **2007**, *39*, 320–327.
- (98) Wang, Y.; Li, Y.; Chen, J.; Zhang, I. Y.; Xu, X. Doubly Hybrid Functionals Close to Chemical Accuracy for Both Finite and Extended Systems: Implementation and Test of XYG3 and XYGJ-OS. *JACS Au* **2021**, *1*, 543–549.
- (99) Zhao, Q.; Martinez, J. M. P.; Carter, E. A. Revisiting Understanding of Electrochemical CO₂ Reduction on Cu(111): Competing Proton-Coupled Electron Transfer Reaction Mechanisms Revealed by Embedded Correlated Wavefunction Theory. *J. Am. Chem. Soc.* **2021**, *143*, 6152–6164.